Chemical Engineering Journal 499 (2024) 155726

Contents lists available at ScienceDirect

Chemical Engineering Journal

journal homepage: www.elsevier.com/locate/cej

Trajectory-based breakup modelling for dense bubbly flows

Christian Weiland [a,*], Alexandra von Kameke [b], Michael Schlüter [a]

[a] Institute of Multiphase Flows, Hamburg University of Technology, Eißendorfer Straße 38, 21073 Hamburg, Germany
[b] Department of Mechanical Engineering and Production Management, Hamburg University of Applied Sciences, Berliner Tor 21, 20099 Hamburg, Germany

ARTICLE INFO

Keywords:
Multiphase flows
Bubble breakup
Trajectory-based methods
Computational fluid dynamics
Bubble size distribution

ABSTRACT

A new model to predict the breakup of gaseous bubbles in a continuous liquid phase is developed. In the model each bubble is modelled as a spring–damper system, namely a Kelvin–Voigt element, while the outer force is derived by a Lagrangian analysis determining the largest stretching rate of the flow field below. The developed model is based on physical principles and no further arbitrary parameters have to be adjusted. Each bubble is observed on its way through the bubbly flow individually, taking into account its history along its respective path. With the implemented model numerical simulations in a wide range of scales are conducted, ranging from the laboratory scale of a vessel of 3 L to the large industrial scale of 15 m^3. The simplicity of the model allows for a good cost to benefit ratio. In the present work, the achieved results are compared to experimental data obtained from optical measurements in a replica of a 200 L aerated stirred tank reactor for various stirrer frequencies.

1. Introduction

Bubbly flows are important in many applications. In oxidation processes for example, oxygen has to be dissolved in the reactive liquid phase. Further, oxygen is of importance in fermentation and cell culture processes to supply cells and microorganisms. Since the relevant chemical and biochemical reactions take place in the liquid phase, the mass transfer from the gaseous phase into the liquid phase is of highest relevance for the whole process. The mass transfer is defined by the mass transfer coefficients and the available interfacial area.

In the Collaborative Research Centre 1615 "SMART Reactors", funded by the German Research Foundation, new reactor types are investigated which will face climate change by operating **S**ustainably, for **M**ultipurpose, **A**utonomously, **R**esiliently, and **T**ransferably. Clearly, for this kind of reactors the prediction of the multiphase fluid dynamics is indispensable and especially the bubble size distribution is dominating in buoyancy driven flows the mixing and the mass transfer.

This work focuses on the development of a breakup model for gaseous bubbles. In the past, many groups have worked on the determination of the bubble size distributions (BSD) which occur during selected processes. In 2009, Liau and Lucas have published two review articles, summarising and classifying many attempts to describe the bubble breakup [1] and the bubble coalescence [2]. Population balance models (PBM) have been proven to perform rather well for predicting BSDs. First mentioned by Hulburt and Katz in 1964 [3] they received ever increasing attention. A detailed book about PBMs was written by Ramkrishna in 2000, delivering an in-depth insight into the mechanism and an overview over the fields of application [4]. More recently, several research groups such as Marchisio et al. and Fox et al. [5–8], Maaß et al. [9,10] or Alopaeus et al. [11–13], just to mention a few, have worked intensively with PBMs, improved and coupled them with Computational Fluid Dynamics (CFD). While PBMs predict the development of a BSD by taking into account the BSD itself and outer acting phenomena, other bubble breakup models, originating in the theory of isotropic turbulence [14], have also been used widely during the past decades. Hinze proposed in 1955 a largest possible drop diameter [15], taking into account quantities such as the turbulent eddy dissipation rate, yielding from the theory of isotropic turbulence. For this purpose, measurements from Batchelor [16] have been used to estimate arising proportionality constants. This relation was later, in 1990, extended and further examined by Kawase and Moo-Young [17] and resulted in a model developed by Martínez-Bazán et al. [18,19] describing both, the breakup frequency and the distribution of daughter bubbles, according to a statistical view. Also in 1990, Prince and Blanch have proposed a phenomenological model to estimate both, the bubble coalescence and breakup in air sparged bubble columns. For this purpose, they have taken into account the bubble–bubble collision rates, the resulting collision efficiencies, and the sizes of turbulent eddies encountering the bubbles, respectively [20]. Luo and Svendson, Lehr et al. and later Xing et al. have taken into account the whole range of turbulent eddies and their contained kinetic energy bombarding the observed

* Corresponding author.
E-mail address: christian.weiland@tuhh.de (C. Weiland).

https://doi.org/10.1016/j.cej.2024.155726
Received 28 May 2024; Received in revised form 21 August 2024; Accepted 10 September 2024
Available online 30 September 2024

Nomenclature

Latin symbols

$\dot{V}_G$	Gas volume flow rate
$\mathcal{T}$	Observed time interval
$\boldsymbol{C}$	Right Cauchy–Green-Strain-Tensor
$\boldsymbol{F}_\sigma$	Surface tension force
$\boldsymbol{F}_{AM}$	Added mass force
$\boldsymbol{F}_{Bu}$	Buoyancy force
$\boldsymbol{F}_D$	Drag force
$\boldsymbol{F}_G$	Gravity force
$\boldsymbol{F}_{Lift}$	Saffman-Lift force force
$\boldsymbol{F}_p$	Pressure force
$\boldsymbol{F}_{t_0}^{t_F}$	Flowmap from t_0 to t_F
$\boldsymbol{I}$	Identity matrix
$\boldsymbol{J}$	Jacobian
$\boldsymbol{S}$	Rate-of-strain tensor
$\boldsymbol{w}$	Velocity
$\boldsymbol{w}_{rel}$	Relative velocity
$\boldsymbol{x}$	Position
a	Smallest semi axis of an ellipsoid
A_{proj}	Projected area
b	Second largest semi axis of an ellipsoid
c	Largest semi axis of an ellipsoid
C_D	Drag coefficient
Co	Courant number
D	Diameter
$d_{R,i}$	Inner reactor diameter
d_S	Stirrer diameter
f_i	Volume fraction of daughter bubble i
g	Gravity of Earth
h	Height
m	Mass
n	Stirrer frequency
p	Pressure
q_0	Number density distribution
R	Radius
S	Surface
t	Time
V	Volume

Greek symbols

η	Dynamic viscosity
λ_3	Largest eigenvalue of the CGST
λ_3^S	Largest eigenvalue of the rate-of-strain tensor
Ω	Geometry
ρ	Density
σ	Interfacial tension
τ_η	Viscous stress
τ_λ	Outer stress
τ_σ	Interface restoring tension
τ_S	Shear stress
θ	Normalised displacement from equilibrium
ε	Eddy dissipation rate
ϑ	Temperature
$\boldsymbol{\gamma}$	Distance between particles

Abbreviations

BSD	Bubble Size Distribution
CRC	Collaborative Research Centre
CFD	Computational Fluid Dynamics
CGST	Right Cauchy–Green-Strain-Tensor
IMS	Institute of Multiphase Flows
LBM	Lattice Boltzmann Method
PBM	Population Balance Model
PBS	Phosphate Buffered Solution
STR	Stirred Tank Reactor
TBBM	Trajectory-Based Breakup Model
TUHH	Hamburg University of Technology

bubble to develop criteria for bubble breakup and give expressions for the resulting daughter size distribution [21–23]. Following the approach of Luo and Svendson, van den Hendel et al. have developed a model to predict the breakup and coalescence of gas bubbles in bubble columns [24]. The group of Kuipers further investigated the Weber number as ratio between inertial and interfacial forces as dominant parameter for the bubble breakup [25,26]. Another attempt to predict the bubble breakup in such vessels was carried out by Mast and Takors, implementing findings from Luo and Svendson [21] and Lehr et al. [22] into selected CFD programmes [27]. Following a different approach, Coulaloglou and Tavlarides developed a correlation, describing the Sauter mean diameter as function of the diameter of a stirred vessel and the Weber number [28], taking into account the turbulent kinetic energy of the bubbles and comparing those with a critical value. Further, several other groups have focused on retrieving or predicting bubble sizes in stirred tanks in dependency of either gaseous or liquid phase properties or geometric characteristics, such as Wilkinson et al. [29], Zhang et al. [30], Zhou and Kresta [31], Martín et al. [32], Alves et al. [33], and Parthasarathy and Ahmed [34]. Tsouris and Tavlarides have improved and combined some of the aforementioned models and used them for the solution of Population Balance Equations [35]. Based on findings of many previously mentioned works, Sarimeseli and Kelbaliyev investigated the deformation of gas bubbles and the influence on the bubble breakup [36]. Further than the aforementioned models, highly resolved numerical simulations have been done for example by Baltussen [37], yielding very detailed information about the breakup of bubbles cut by a wire. The knowledge from those simulations can be applied to give more insight into the breakup process itself. A direct implementation of these highly resolved simulation to large scale systems on the other hand, is not possible due to the high computational cost.

While many of the models that do predict BSDs have either the necessity to solve integrals, which can be numerically expensive, or to determine proportionality constants which arise in the development of the correlation models, this work follows a different approach.

In this work, each and every bubble present in an observed system is treated individually. The bubbles' deformations are computed along their respective trajectory, hence the history of each bubble with regard to the local conditions is taken into account. The relevance of the history of a fluid particle along its trajectory has already been shown by Nachtigall et al. [38] for droplets. Further, Risso et al. and Lalanne et al. [39,40] have formulated a differential equation, describing the bubble deformation along its trajectory by taking into account the velocity fluctuations in the near-bubble area. Vela-Martín and Avila have linked the energy a droplet or bubble gains or loses on its way along the respective trajectory to the rate of strain or the rate of compression, respectively, obtainable from the rate-of-strain tensor [41]. The work stresses the effect of the history of deformation of the bubble onto its breakup behaviour. The deformation and the consecutive breakup of

single bubbles in a quiescent medium and in artificial turbulence were also recently observed experimentally and reviewed by the group of Ni et al. in a very detailed way [42–45]. This group has conducted experiments in which they recorded the shape and deformation of bubbles with multiple cameras and a high resolution. The results are then used to extend an existing model for the evolution of the elliptical bubble shape and its orientation along its trajectory developed by Maffettone and Minale [46]. Ni et al. introduced additional terms into the model that take into account the slip velocity between bubble and carrier fluid as well as the coarse grained strain [47,48]. Further, the deformation and breakup of gas bubbles have also been investigated by Zedníková et al. [49,50].

To take into account the effect of the carrier flow on the bubble deformation in this work, the bubbles are assumed to behave like Kelvin–Voigt elements, first mentioned by William Thomson, 1st Baron Kelvin and Voigt [51,52] and used for the description of plastic material properties and rheological phenomena. The modelling of bubbles as Kelvin–Voigt element has already been proposed by Lagisetty et al. [53] and Nambiar et al. [54], where the breakup criteria was derived from global variables such as the stirrer speed in the case of stirred vessels. In this work, the local phenomena of the carrier fluid causing the bubble deformation are based on Lagrangian deformation theory, which has been intensively studied during the last decades to analyse transport barriers especially in oceanographic flows [55,56], but has also been applied to multi- and singlephase flows recently [57–60], which are relevant for chemical or biochemical processes. In the proposed model, namely the Trajectory-Based Breakup Model (TBBM), the size of the daughter bubbles is retrieved by conserving the energy the bubble has gained due to deformation. Altogether, the TBBM is based on first principles from physics and mathematics. Neither fitting constants have to be determined by fitting data, nor tedious or computationally expensive integrals have to be solved. Summarising, in the development of the TBBM the following assumptions are made:

- Every bubble is a prolate ellipsoid with an initial spherical shape and is modelled with a Kelvin–Voigt element. This might lead to errors when strictly wobbling bubbles or oblate ellipsoidal bubbles are to be expected, compare Clift et al. [61].
- The tension which is relevant for the deformation is only based on the largest strain the bubble experiences at its position and the bubble rotates immediately in a way that it is always deformed in the same, initial direction, which could lead to a slight overprediction of the deformation, hence an overprediction of the breakup rate could occur.
- The bubble breaks in the very moment in which it is so strongly deformed that the interfacial force is smaller than the inertial forces. Since the deformation of the bubbles already take into account the time leading to the breakup this assumption is deemed to not be very error prone.
- Every bubble which breaks undergoes a binary breakup while the daughter bubbles conserve the energy of the mother bubble in its deformed state. This assumption will lead to slight errors where ternary or higher order breakup is relevant. Those errors are not expected to be too large, since the observed bubble could potentially break again in a rather short time, leading to a pseudo higher order breakup.

Measures to encounter the limitations introduced with those assumptions in future works are summarised in Section 4 at the end of this article. The TBBM is implemented and tested using M-Star CFD (M-Star Simulations, LCC.) for a wide range of scales, ranging from the small scale of 3 L, containing about a hundred bubbles at a point in time, to the large scale of 15 m^3, containing about a million bubbles at a point in time. The validation shown in this work is limited to a mid-size stirred tank reactor with a working volume of 200 L. The model is validated with experimental data and compared with the default model in M-Star CFD based on the critical diameter defined by Kawase and Moo-Young [17] coupled with a statistical expression for the daughter size distribution by Xing et al. [23] as described by Thomas et al. [62].

2. Material and methods

First, the forces acting on a gaseous bubble are described and classified into advecting, stabilising and destabilising forces. Afterwards, those forces are further processed into a model to predict the bubble breakup, taking into account the history of the bubble. Finally, the geometry of the test case and the implementation of the model are presented.

2.1. Forces acting on bubbles in bubbly flows

Gaseous bubbles in a liquid flow experience several forces. These forces are either acting on the movement of the respective bubble through the observed apparatus or are responsible for changes of the bubble's shape and orientation. The forces which are connected to the deformation can also be responsible for the bubble breakup. Simplifying the bubble as point mass, the forces which are connected to the movement of the bubble are the gravitational force $\boldsymbol{F}_{\mathrm{G}}$, the buoyancy force $\boldsymbol{F}_{\mathrm{Bu}}$, the Saffman-Lift force $\boldsymbol{F}_{\mathrm{Lift}}$ [63], the added mass force $\boldsymbol{F}_{\mathrm{AM}}$ [64] and the drag force $\boldsymbol{F}_{\mathrm{D}}$ [65]. Further, the history of the bubble along its trajectory namely its de- and acceleration have an influence on its movement. This influence can be taken into account by the Basset history force $\boldsymbol{F}_{\mathrm{Basset}}$ [66]. In the model shown in this paper, the Basset history force is neglected in a first step in order to save computational costs. Consequently, the motion of the bubble is described by Newton's second law

$$m_{\mathrm{B}}\ddot{\boldsymbol{x}}_{\mathrm{B}} = \boldsymbol{F}_{\mathrm{G}} + \boldsymbol{F}_{\mathrm{Bu}} + \boldsymbol{F}_{\mathrm{Lift}} + \boldsymbol{F}_{\mathrm{AM}} + \boldsymbol{F}_{\mathrm{D}}. \tag{1}$$

Hereby, m_{B} and $\boldsymbol{x}_{\mathrm{B}}$ are the bubble's mass and its position, respectively, the dot indicates the derivative with respect to time. Further, Newton's third law is applied, the forces acting from the continuous phase on the bubble are also acting from the bubble on the continuous phase for taking into account the two way coupling. This results in a change of velocity of the fluid directly surrounding the bubble.

While the upper mentioned forces act directly on the movement of the bubble, additional forces have to be taken into account to describe the dynamic changes of the bubble shape and orientation. For a detailed description of the forces and tensions influencing the bubble size and shape, the reader is referred to the textbook written by Clift et al. [61], who classified bubbles over a large range of conditions, summarised in the famous Clift–Grace–Weber diagram. In general, the forces can be characterised as either stabilising or destabilising forces. The most dominant stabilising force is induced by the interfacial tension σ. The interfacial tension can be used to calculate the pressure difference between the observed gas bubble and the surrounding liquid, yielding the Young–Laplace equation [67]

$$\Delta p = \frac{2\sigma}{R} \equiv \frac{4\sigma}{D}, \tag{2}$$

where R and D are the spherical bubble's radius and diameter, respectively. Further information about the occurring forces can be obtained from the free body diagram given in Fig. 1. The pressure force in the relevant direction

$$F_p = \Delta p \cdot \frac{\pi}{4} D^2. \tag{3}$$

is equivalent to the pressure difference multiplied by the projected surface area of the half bubble. In the case that the observed bubble is in equilibrium, the forces have to be equal, such that

$$F_p = \Delta p \cdot \frac{\pi}{4} D^2 \overset{!}{=} \frac{4\sigma}{D} \cdot \frac{\pi}{4} D^2 = \sigma \pi D = F_\sigma \tag{4}$$

can be retrieved directly from the Young–Laplace equation as force induced by the interfacial tension for the case of a spherical bubble. This stabilising force, which is responsible to keep the observed bubble in a spherical shape, has to be overcome to deform and eventually break the bubble. Since the obtained interfacial tension force is acting on the whole surface of the gas bubble S_{B}, it is further processed into the

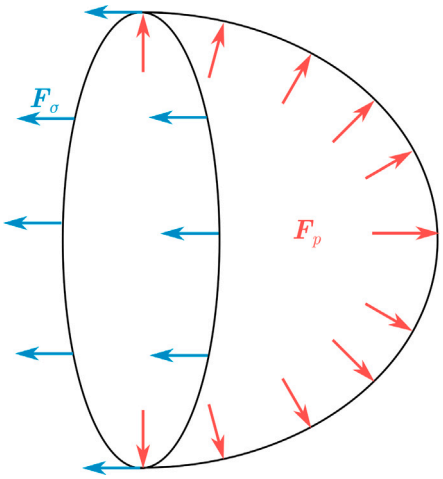

Fig. 1. Free body diagram of half a bubble with the pressure force F_p and the force through interfacial tension F_σ.

interface restoring tension by dividing the interfacial tension force by the total surface area of the gas bubble

$$\tau_\sigma := \frac{F_\sigma}{S_\mathrm{B}} = \frac{\pi\sigma D}{\pi D^2} = \frac{\sigma}{D} \equiv \frac{\sigma}{2R}. \tag{5}$$

This was also reported by Hinze [15].

After analysing the force which stabilises gas bubbles, the counterpart, the destabilising forces, are examined. When a gaseous bubble is advected in a flow, inertial or shear forces may act on the bubble and imply a deformation. These forces occur either by velocity gradients, e.g., turbulent eddies or by the relative motion between the continuous and the dispersed phase, inducing a drag. When observing turbulent eddies, only those are considered relevant for the deformation, which are of the same or smaller size than the observed bubbles [21] and contain a sufficient amount of energy to overcome the interfacial tension. The drag force acting on a gas bubble

$$\boldsymbol{F}_\mathrm{D} = C_\mathrm{D} \cdot \frac{\rho}{2} \cdot A_\mathrm{proj} \cdot \|\boldsymbol{w}_\mathrm{rel}\|_2 \cdot \boldsymbol{w}_\mathrm{rel} \tag{6}$$

depends on the relative velocity $\boldsymbol{w}_\mathrm{rel} := \boldsymbol{w} - \boldsymbol{w}_\mathrm{B}$ between the bubble and the surrounding fluid, the density of the fluid ρ, the projected area of the bubble A_proj and the drag coefficient C_D which depends on the flow regime and the geometry of the bubble [68]. These phenomena eventually yield into shear forces [17]

$$\tau_\mathrm{S} \propto \rho \|\boldsymbol{w}\|_2^2, \tag{7}$$

which act tangentially on the surface of the bubble, resulting in a force which deforms the bubble and counteracts the surface restoring force. In the regions where the Kolmogoroff energy distribution law is valid, Batchelor showed a dependency

$$\|\boldsymbol{w}\|_2^2 = C_1 \cdot (\varepsilon D)^{\frac{2}{3}}, \tag{8}$$

which takes the turbulent energy dissipation rate ε into account [15,16] with a proportionality constant $C_1 \in \mathbb{R}^+$. From Eqs. (5) and (8), a dependency of the largest stable bubble diameter can be calculated as reported by Kawase and Moo-Young by setting both stresses equal [17]

$$\tau_\sigma = \frac{\sigma}{D} \overset{!}{=} C_1 \cdot \rho (\varepsilon D)^{\frac{2}{3}} = \tau_\mathrm{S} \tag{9}$$

$$\Rightarrow D_\mathrm{max} = C_2 \cdot \frac{\sigma^{\frac{3}{5}}}{\rho^{\frac{3}{5}} \cdot \varepsilon^{\frac{2}{5}}} \tag{10}$$

with a proportionality constant $C_2 \in \mathbb{R}^+$. This is, under consideration of the theory of isotropic turbulence, the largest possible bubble diameter at a specific position at a specific point in time. This classical formulation for bubble breakup will be compared to the model developed in this research work. Eq. (10) was used by Martínez-Bazán et al. [18] to develop a model which describes the bubble breakup and takes also different daughter bubble sizes into account [19]. In the course of the shown mechanism one major assumption was made: A bubble breaks immediately when the bubble diameter exceeds the maximal possible diameter. This, on the other hand, is not possible since an infinite amount of energy would be necessary for this to happen. The breakup of a gaseous bubble or a liquid droplet has to be a dynamic process which occurs over a specific amount of time [38]. The modelling of this phenomenon is the goal of this work and will be presented in Section 2.3.

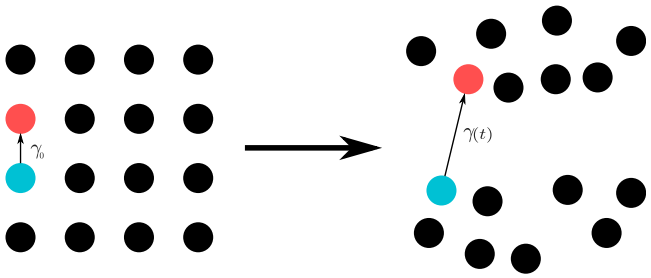

Fig. 2. Schematic positions of particles at the initial time t_0 (left) and at the later time t (right) [60].

2.2. Deformation of Lagrangian fluid elements

This section gives only a brief insight into the deformation of Lagrangian fluid elements, a more detailed description was given by Haller [55,69]. Let $\boldsymbol{w} \in C^2$ denote the velocity field of a fluid inside a given geometry $\Omega \subseteq \mathbb{R}^3$ for a given time interval $\mathcal{T} \subseteq \mathbb{R}$. It is assumed that fluid elements or non-inertial point particles will follow the flow perfectly. The trajectory $\boldsymbol{x}(t) \in \Omega,\ t \in \mathcal{T}$ of a fluid element or point particle and thus of every passive tracer is obtained via the solution of the initial value problem

$$\dot{\boldsymbol{x}}(t) = \boldsymbol{w}(\boldsymbol{x}(t), t), \quad \boldsymbol{x}(t_0) = \boldsymbol{x}_0 \tag{11}$$

leading to

$$\boldsymbol{x}(t) = \boldsymbol{x}_0 + \int_{t_0}^{t} \boldsymbol{w}(\boldsymbol{x}(\tau), \tau)\,\mathrm{d}\tau,\ t \in \mathcal{T}. \tag{12}$$

The flow map $\boldsymbol{F}_{t_0}^{t_\mathrm{F}} : \Omega \to \Omega$ is the solution operator, which maps tracers from their position $\boldsymbol{x}_0$ at time t_0 onto their new position $\boldsymbol{x}_\mathrm{F}$ at a later, final time t_F according to Eq. (12), hence $\boldsymbol{F}_{t_0}^{t_\mathrm{F}}(\boldsymbol{x}_0) = \boldsymbol{x}(t_\mathrm{F})$. For means of clarity the indices and arguments of the flow map are omitted in the following.

For two passive particles i and j, their distance vector at time $t \in \mathcal{T}$

$$\boldsymbol{\gamma}(t) := \boldsymbol{x}_j(t) - \boldsymbol{x}_i(t) \tag{13}$$

is considered. The evolution of the distance $\boldsymbol{\gamma}(t)$ is depicted schematically in Fig. 2 and as long as the distance is sufficiently small it evolves as

$$\boldsymbol{\gamma}(t_\mathrm{F}) = \boldsymbol{J}_{\boldsymbol{F}} \cdot \boldsymbol{\gamma}_0 \tag{14}$$

with an initial distance $\boldsymbol{\gamma}_0$ at time t_0 [70]. Hereby $\boldsymbol{J}_{\boldsymbol{F}}$ denotes the Jacobian of the flow map. In other words: An initial deviation $\boldsymbol{\gamma}_0$ between particles around position $\boldsymbol{x}_0$ at time t_0 will be transformed linearly by the Jacobian of the flow map to another deviation $\boldsymbol{\gamma}(t_\mathrm{F})$ between the same particles at time t_F. For means of clarity, the argument t_F in $\boldsymbol{\gamma}(t_\mathrm{F})$ will be omitted. Any matrix $\boldsymbol{A} \in \mathbb{R}^{n\times n}$ can be decomposed into an orthogonal matrix $\boldsymbol{Q} \in \mathbb{R}^{n\times n}$ and a symmetric positive (semi) definite matrix $\boldsymbol{R} \in \mathbb{R}^{n\times n}$ [71]. Since this work deals with problems where continuity holds, the matrix $\boldsymbol{R}$ has a determinant of $\det \boldsymbol{R} = 1$ [72],

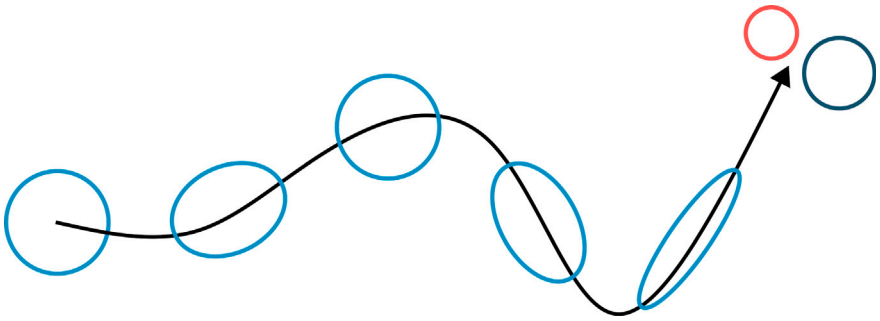

Fig. 3. Deformation of a gaseous bubble along its trajectory, eventually leading to breakup.

hence it is definite. This polar decomposition can be used on the Jacobian of the flow map

$$\boldsymbol{J_F} = \boldsymbol{QR} \Rightarrow \boldsymbol{\gamma} = \boldsymbol{QR} \cdot \boldsymbol{\gamma}_0. \tag{15}$$

The matrix $\boldsymbol{R}$ is responsible for deformation due to stretching, shrinking, and shear, thus increasing or decreasing the magnitude of an initial deviation $\boldsymbol{\gamma}_0$. The matrix $\boldsymbol{Q}$ on the other hand is responsible for pure rotation. To be able to state which degree of deformation occurs, the inner product

$$\boldsymbol{\gamma}^T\boldsymbol{\gamma} = \boldsymbol{\gamma}_0^T \cdot \left(\boldsymbol{J_F}\right)^T \boldsymbol{J_F} \cdot \boldsymbol{\gamma}_0 = \boldsymbol{\gamma}_0^T \boldsymbol{R}^T \underbrace{\boldsymbol{Q}^T\boldsymbol{Q}}_{\equiv \boldsymbol{I}} \boldsymbol{R}\boldsymbol{\gamma}_0 = \boldsymbol{\gamma}_0^T \underbrace{\boldsymbol{R}^T\boldsymbol{R}}_{=:\boldsymbol{C}} \boldsymbol{\gamma}_0 \tag{16}$$

can be set up. Hereby $\boldsymbol{C} \equiv \left(\boldsymbol{J_F}\right)^T \boldsymbol{J_F}$ is the Right Cauchy–Green-Strain-Tensor (CGST) [73]. From the CGST, a quantitative value for the largest stretch at the observed position $\boldsymbol{x}_0$ is achieved by finding the eigenvector $\boldsymbol{\zeta}_3$ corresponding to the largest eigenvalue $\sqrt{\lambda_3}$ of $\boldsymbol{R}$ and setting the vector $\boldsymbol{\gamma}_0$ equal to it, such that

$$\boldsymbol{\gamma}^T\boldsymbol{\gamma} = \lambda_3 \boldsymbol{\gamma}_0^T\boldsymbol{\gamma}_0 \Rightarrow \sqrt{\frac{\boldsymbol{\gamma}^T\boldsymbol{\gamma}}{\boldsymbol{\gamma}_0^T\boldsymbol{\gamma}_0}} = \sqrt{\lambda_3} \tag{17}$$

holds. This is the largest deformation at the observed position after the integration time $\Delta t := t_\mathrm{F} - t_0$. When the time interval becomes sufficiently small the CGST can be approximated by a function of the Eulerian strain tensor which describes the local, instantaneous deformation a fluid parcel experiences at a given instant [74]. This will be used as detailed below in Section 2.3.

2.3. The Trajectory-Based Breakup Model

To derive the core of this work, the TBBM taking into account the history of a gaseous bubble along its trajectory, compare Fig. 3, the aforementioned mechanisms are combined. For this purpose, a gaseous bubble is assumed to firstly be of spherical shape and becoming ellipsoidal due to deformation. Also, the bubble is assumed to behave like a Kelvin–Voigt [51,52] element. All deformation and breakup processes will take place with respect to volume conservation, such that

$$V_\mathrm{B} \equiv V_\mathrm{Sphere} = \frac{4\pi}{3} R^3 = \text{const.} \tag{18}$$

holds.

2.3.1. Approximation of bubble shape, volume, and surface

In this work bubbles are approximated as ellipsoids. For a sphere with the radius R the surface is

$$S_\mathrm{B,Sphere} = 4\pi R^2, \tag{19}$$

while for an ellipsoid two cases have to be differentiated for which first the dimensions have to be defined. An ellipsoid has three principal semi axis a, b, and c with $0 < a \leq b \leq c$ and its volume is

$$V_\mathrm{Ellipsoid} = \frac{4\pi}{3} abc. \tag{20}$$

For the case $a = b = c \equiv R$ the ellipsoid is a sphere. In this work only rotational ellipsoids are taken into account, thus $a = b$ or $b = c$. For the case that $a = b$ the ellipsoid is prolate, for the other case it is oblate. The surface of a prolate ellipsoid is [75]

$$S_\mathrm{Prolate} = 2\pi a \left(a + \frac{c^2}{\sqrt{c^2 - a^2}} \cdot \arcsin\left(\frac{\sqrt{c^2 - a^2}}{c} \right) \right) \tag{21}$$

and the surface of an oblate ellipsoid is [75]

$$S_\mathrm{Oblate} = 2\pi c \left(c + \frac{a^2}{\sqrt{c^2 - a^2}} \cdot \operatorname{arsinh}\left(\frac{\sqrt{c^2 - a^2}}{a^2} \right) \right). \tag{22}$$

In this work the prolate breakup is considered the most relevant. Oblate and more complex breakup is still under study and can be added to the model later. For the constraint of volume conserving

$$R^3 = a^2 c \Rightarrow a = \sqrt{\frac{R^3}{c}} \tag{23}$$

has to hold during the whole process, thus

$$S_\mathrm{Prolate}(c) = 2\pi \cdot \sqrt{\frac{R^3}{c}} \cdot \left(\sqrt{\frac{R^3}{c}} + \frac{c^2}{\sqrt{c^2 - \frac{R^3}{c}}} \cdot \arcsin\left(\frac{\sqrt{c^2 - \frac{R^3}{c}}}{c} \right) \right). \tag{24}$$

In the TBBM the surface will change continuously in each time step due to the deformations the bubble experiences until it becomes unstable, eventually leading to bubble breakup.

2.3.2. Modelling of the bubble shape and breakup

The observed bubble is modelled as Kelvin–Voigt element, consisting of a parallel connection of a spring and a damper, compare Fig. 4. This attempt was already proposed by Nambiar et al. and Lagisetty et al. [53,54]. The damper mirrors the influence of the bubble's viscous movement, depicted by the viscous stress τ_η and the bubble's capability to absorb energy, while the spring mirrors the influence of the interfacial tension, depicted by the interfacial tension stress τ_σ when the bubble is exposed to an outer disturbance or an outer stress τ_λ. Following this approach, an equation taking into account these different stresses

$$\tau_\lambda = \tau_\sigma + \tau_\eta \tag{25}$$

can be formulated, being the basis of the TBBM. For the interfacial tension stress the equivalent from Section 2.1 is used, hence

$$\tau_\sigma = \frac{\sigma}{2a} \cdot \theta \tag{26}$$

with $\theta := \frac{c-R}{R}$ as normalised displacement from the equilibrium $c = R$ [54] of the undisturbed system with $\tau_\lambda = 0$. Hereby, a is the minor semi axis of the prolate ellipsoid. The viscous stress is

$$\tau_\eta = \eta_\mathrm{B} \cdot \frac{\mathrm{d}\theta}{\mathrm{d}t} = \eta_\mathrm{B} \cdot \frac{1}{R} \cdot \frac{\mathrm{d}c}{\mathrm{d}t} \approx \eta_\mathrm{B} \cdot \frac{1}{R} \cdot \frac{\Delta c}{\Delta t}, \tag{27}$$

where Δc is the difference of the major semi axis c during a specified time interval Δt and η_B is the viscosity of the gas forming the bubbles.

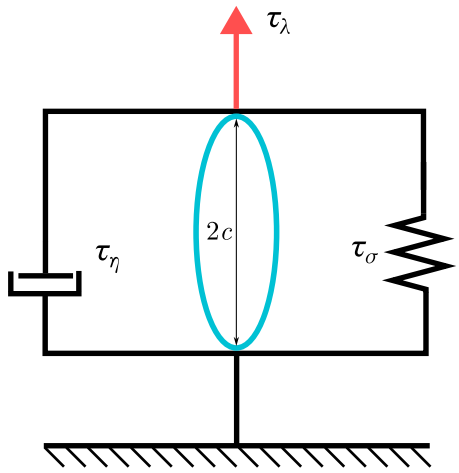

Fig. 4. Model of the gaseous bubble as Kelvin–Voigt element.

In this work, the time interval Δt is the time step size of the numerical simulation and hence is in the order of microseconds.

Finally, the outer stress causing the bubble to deform arises from the Eulerian rate of strain, described by the rate-of-strain tensor $\boldsymbol{S} := 1/2 \cdot \left(\boldsymbol{J_w} + \boldsymbol{J_w}^T\right)$, where $\boldsymbol{J_w}$ is the Jacobian of the Eulerian velocity field $\boldsymbol{w}$. Here, it is proposed that the largest rate of stretch is the main driver for the bubble deformation which eventually causes the break up [45,76] and thus the outer stress is formulated using the largest eigenvalue of the rate-of-strain tensor $\lambda_3^{\boldsymbol{S}}$

$$\tau_\lambda = \eta_\mathrm{F} \cdot \lambda_3^{\boldsymbol{S}} \tag{28}$$

with η_F being the liquid's dynamic viscosity. Serra and Haller [74] have shown that the rate-of-strain tensor and the CGST are related as

$$\boldsymbol{C} = \boldsymbol{I} + 2\boldsymbol{S} \cdot \Delta t + \mathcal{O}\left(\Delta t^2\right). \tag{29}$$

Therefore the largest eigenvalue λ_3 of the CGST for small Δt can be directly related to the largest eigenvalue $\lambda_3^{\boldsymbol{S}}$ of the Eulerian strain tensor, namely, $\lambda_3^{\boldsymbol{S}} = \frac{\lambda_3 - 1}{2\Delta t}$, which leads to

$$\tau_\lambda = \eta_\mathrm{F} \cdot \frac{\lambda_3 - 1}{2\Delta t}. \tag{30}$$

In this work, the CGST rather than the rate-of-strain tensor is used due to its beneficial property as symmetric, positive definite matrix for eigenvalue calculation, while the rate-of-strain tensor is unconditionally indefinite.

Inserting all stresses into Eq. (25) leads to the final equation of the TBBM coupled with the Eulerian rate of strain as outer stress described via the largest eigenvalue of the CGST

$$\eta_\mathrm{F} \cdot \frac{\lambda_3 - 1}{2\Delta t} = \frac{\sigma}{2aR} \cdot (c - R) + \eta_\mathrm{B} \cdot \frac{1}{R} \cdot \frac{\Delta c}{\Delta t} \tag{31}$$

to describe the deformation of the observed gaseous bubble by its major semi axis c along its way through the bubbly flow. Since the local and instantaneous CGST is used here, effects such as the intermittency phenomenon [77] should be better accounted for as in models utilising isotropic turbulence. In comparison to the FBD, a phenomenological model on the deformation and orientation dynamics, described in the work of Masuk et al. [48], the TBBM appears rather simple. While the FBD gives detailed information on the 3D orientation and all axes of an ellipsoid, the TBBM considers the length changes of the major axis and also quietly assumes an instantaneous redirection of the major axis into the direction of largest stretch, which is considered to be the dominant mechanism for deformation in the applications observed in this work. Additionally, this simplifications also speed up the calculation. The TBBM is easily implemented, but two way coupling should be taken into account when the bubbles trajectories are calculated as described in Section 2.1. This necessity arises since the TBBM itself does not take into account any effects that the mismatch between the flow and the bubble velocity might have onto the outer stress or any effects that the bubble might have on the strain field. Therefore the outer stress and the rate-of-strain tensor that affect the stretching should already include the effect that the bubble has on the local flow surrounding it as precisely as possible. This should reduce the local slip velocity and thus its direct influence on the bubble deformation which plays a major role in the FBD where, in contrast, two way coupling does not have to be considered. Another difference is the main property which is modelled. While the rate of compression is focused on in the work of Masuk et al. hence it lays on oblate ellipsoids, the largest stretch, and thus prolate deformation is modelled in this work. This is done due to the assumption that this is dominant in the near stirrer region inside of STRs, which are the apparatuses of interest in this work and the main part of bubble breakup takes place here.

To formulate a criterion that determines if the deformation leads to bubble breakup or not, the interfacial tension force is compared to the drag force, which was proposed by Mersmann [78]. For the case that

$$F_\sigma = 2\pi a\sigma = 2\pi \cdot \sqrt{\frac{R^3}{c}} \cdot \sigma < \left\|\boldsymbol{F}_\mathrm{D}\right\|_2 \approx V_\mathrm{B} \cdot g \cdot \left(\rho_\mathrm{F} - \rho_\mathrm{B}\right) \tag{32}$$

the bubble will disintegrate as the result of the interfacial tension not being able to stabilise the bubble anymore against the inertial forces. The drag force is approximated by taking into account the buoyancy force, following the approach of Mersmann estimating the largest stable bubble diameter. In this model it is assumed that the result of a breakup event are two initially spherical daughter bubbles with the radii R_1 and R_2, respectively.

Finally, a description of the size of the daughter bubbles is needed. During its lifetime, the mother bubble (no index) has experienced some energy gain or energy loss, which can be stated in terms of surface energy [41]

$$E = \sigma \cdot S. \tag{33}$$

For this model, the surface energy is assumed to be contained such that

$$\sigma \cdot S = \sigma \cdot \left(S_1 + S_2\right) \Leftrightarrow S = S_1 + S_2. \tag{34}$$

Further, mass conservation has to be fulfilled, which leads to a conservation of the total volume, such that

$$V = V_1 + V_2. \tag{35}$$

With the volume fraction of the first daughter bubble

$$f_1 := \frac{V_1}{V} \equiv \left(\frac{R_1}{R}\right)^3 \tag{36}$$

and the volume fraction of the second daughter bubble

$$f_2 := \frac{V_2}{V} \equiv 1 - f_1 \tag{37}$$

the total surface area after the breakup is

$$S_1 + S_2 = 4\pi R^2 \left(f_1^{\frac{2}{3}} + \left(1 - f_1\right)^{\frac{2}{3}}\right). \tag{38}$$

Coming back to the energy conservation and calculating the surface area of the deformed mother bubble yields

$$2\pi \cdot \sqrt{\frac{R^3}{c}} \cdot \left(\sqrt{\frac{R^3}{c}} + \frac{c^2}{\sqrt{c^2 - \frac{R^3}{c}}} \cdot \arcsin\left(\frac{\sqrt{c^2 - \frac{R^3}{c}}}{c}\right)\right) = 4\pi R^2 \left(f_1^{\frac{2}{3}} + \left(1 - f_1\right)^{\frac{2}{3}}\right), \tag{39}$$

which has to be fulfilled by the energy and mass conserving volume fraction $f_1 \in (0, 0.5]$ and finalises the TBBM, the proposed model for the bubble breakup taking into account its history and only first principles along its trajectory without the need of further fitting parameters.

2.3.3. Model implementation

To test and validate the model, it is implemented in M-Star CFD (M-Star Simulations, LCC.) by writing user-defined functions in the language C. M-Star CFD is a commercial programme utilising the Lattice Boltzmann Method (LBM). For deeper insight into the LBM the reader is advised to the books written by Krüger et al. [79] or Succi [80].

Since only the largest eigenvalue λ_3 of the CGST is needed, the power method [81] is implemented for the determination of this value and is conducted at each lattice point for one numerical time step Δt. The code for this purpose can be found in Appendix E. For each bubble i the major semi axis c_i is calculated with initial conditions $c_i = R_i$ at $t_{0,i}$ individually according to the code in Appendix F. Hereby $t_{0,i}$ is the time at which the respective bubble i enters the domain, either by addition at the gas inlet or by birth due to bubble breakup or coalescence. R_i is the radius of the spherical bubble i. With the value of the major semi axis the deformation for each bubble i is quantified and used to check whether the breakup criterion defined in Eq. (32) is met or not. For the case it is met, the volume fraction of the first daughter bubble is calculated according to Eq. (39), cf. the code in Appendix G.

2.4. Stirred tank reactor setup (STR) and process conditions

As geometry for validation a transparent replica of the BIOSTAT STR® 200 from Sartorius Stedim Biotech GmbH is used. The physical BIOSTAT STR replica is made of acrylic glass to enable optical access. The reactor is located at the Institute of Multiphase Flows (IMS) of Hamburg University of Technology (TUHH). It has an inner diameter of $d_{\mathrm{R,i}} = 590\,\mathrm{mm}$ and a total height of 1003 mm. The working volume is $V_{\mathrm{R}} = 200\,\mathrm{L}$. The STR is further equipped with three tubes, acting as baffles and two segment stirrers with a diameter of $d_{\mathrm{S}} = 224\,\mathrm{mm}$ and a distance between the stirrers of $\Delta h_{\mathrm{S}} = 300\,\mathrm{mm}$ and is aerated via a ring sparger with in total 20 circular holes with a diameter of $d_{\mathrm{H}} = 0.8\,\mathrm{mm}$. The STR is depicted schematically in Fig. 5. As liquid phase deionised water (DI water) with a phosphate buffered solution (PBS) is used and pressurised air as gaseous phase. For this setup detailed experimental measurements have been conducted at the IMS. As physical properties the values for a temperature of $\vartheta = 37\,^{\circ}\mathrm{C}$ were used. The interfacial tension is $\sigma = 0.069\,\mathrm{N\,m^{-1}}$, the liquid phase's density is $\rho_{\mathrm{L}} = 998.2\,\mathrm{kg\,m^{-3}}$ and the one of the gaseous phase is $\rho_{\mathrm{B}} = 1.204\,\mathrm{kg\,m^{-3}}$. The liquid phase's dynamic viscosity is $\eta_{\mathrm{L}} = 7.9 \cdot 10^{-4}\,\mathrm{Pa\,s}$ and the gaseous phase's dynamic viscosity is $\eta_{\mathrm{B}} = 17.2 \cdot 10^{-6}\,\mathrm{Pa\,s}$. The aeration rate is $\dot{V}_{\mathrm{G}} = 20\,\mathrm{L\,min^{-1}}$ (norm litre) and the stirrer frequency is $n \in \{50\,\mathrm{rpm}, 100\,\mathrm{rpm}, 150\,\mathrm{rpm}\}$. The initial bubble size was estimated as $d_{\mathrm{initial}} = 0.01\,\mathrm{m}$ for the simulations. A numerical grid of $400 \times 565 \times 425$ lattice points was found to resolve the flow sufficiently by convergence testing, compare Fig. 8 in Appendix A. As coalescence model the M-Star default model [82] based on a critical approach Reynolds number [83] of $Re_{\mathrm{crit}} = 40$ was used. The time step size Δt is adjusted case dependent to guarantee $Co \leq 0.05,\ \forall \boldsymbol{x} \in \Omega, t \in \mathcal{T}$. For each case a simulation time of one minute was chosen.

3. Model validation

The developed model is applied to the STR geometry and the process conditions described in Section 2.4. The validation is performed qualitatively by comparing the visual image of the bubbly flow and quantitatively by comparing the bubble size distributions of the simulation and the experiment in the region comprised by a red dashed line in Fig. 5. The experimental BSDs are obtained by manually evaluating high-resolution photos taken with a camera (Nikon D7500) and a lens (Carl Zeiss ZF Planar f 1.4 50 mm). First, in Fig. 6 the bubble images for the stirrer frequencies $n \in \{50\,\mathrm{rpm}, 100\,\mathrm{rpm}, 150\,\mathrm{rpm}\}$ and a gas volume flow rate of $\dot{V}_{\mathrm{G}} = 20\,\mathrm{L\,min^{-1}}$ (norm-litre) are shown. The simulations are carried out on two NVIDIA H100 Tensor-Core GPUs and take between four and eleven hours for one minute simulated time, dependent on the stirrer frequency. The necessary video memory is rather low. The data connected directly to the bubbles take up about 1 GB of storage for ca. 100000 bubbles, while the total available memory on two NVIDIA H100 Tensor-Core GPUs is 160 GB. In the simulation of the presented set-up between four and twelve minutes of wall time were needed for one simulated second, depending on the stirrer frequency. The usage of more GPUs should reduce the necessary wall time. From just a visible inspection the simulative images show two phase flow patterns resembling largely those from the experiment. For all three simulated cases the main properties of the respective experimental two phase flows are well represented. The bubbles rise mostly in the centre part of the STR for a stirrer frequency of $n = 50\,\mathrm{rpm}$. For a stirrer frequency of $n = 100\,\mathrm{rpm}$ both the experiment and the simulation show a necking between the two stirrers and a broader distribution above the top stirrer. Further, for a stirrer frequency of $n = 150\,\mathrm{rpm}$ bubbles are completely distributed over the whole STR for experiment and simulation. Overall, some differences between the images from simulation and experiment remain but the core characteristics of the two phase flows are mirrored satisfactorily by the simulations. This comparison does not only show the capabilities of the proposed model, but also the capabilities of M-Star CFD to predict the flow pattern of a multiphase flow for different process conditions regarding whether the stirrer is flooded or not and how well the bubbles are distributed. This accuracy is only possible if the bubble sizes, which are responsible for the buoyancy driven flows, are calculated correctly. A closer look on individual trajectories is given in Fig. 11 in Appendix D. Shown are the trajectories of two bubbles initially injected at the sparger and the ones of all their children. While at the lower stirrer a breakup event can hardly be seen visually due the high amount of breakup events happening here, it can be seen clearly at the upper stirrer.

A more detailed validation is therefore conducted by comparing the bubble size distributions from the experiments with the simulations for both the utilisation of the TBBM and the model proposed by Kawase and Moo-Young [17] coupled with the daughter size distribution proposed bei Xing et al. [23] in the region for validation (red box in Fig. 5). The presented distributions include the data evaluated each second over 40 s. A statistical convergence analysis showed that at least four sets of data should be taken into account to yield converged statistics. Combined with the necessary wall time for one simulated

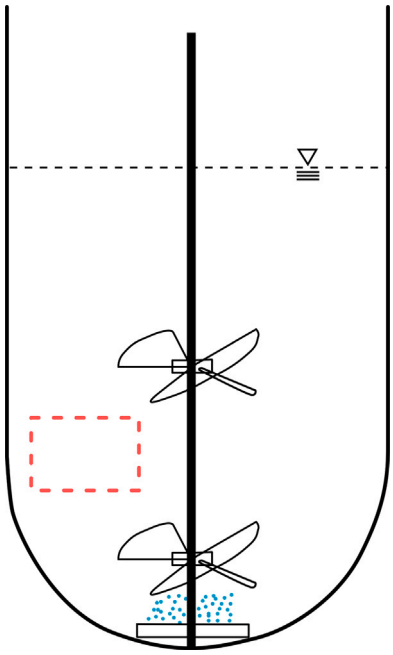

Fig. 5. Schematic depiction of the BIOSTAT STR® 200 replica with region for validation of the bubble size distribution comprised by red dashed line.

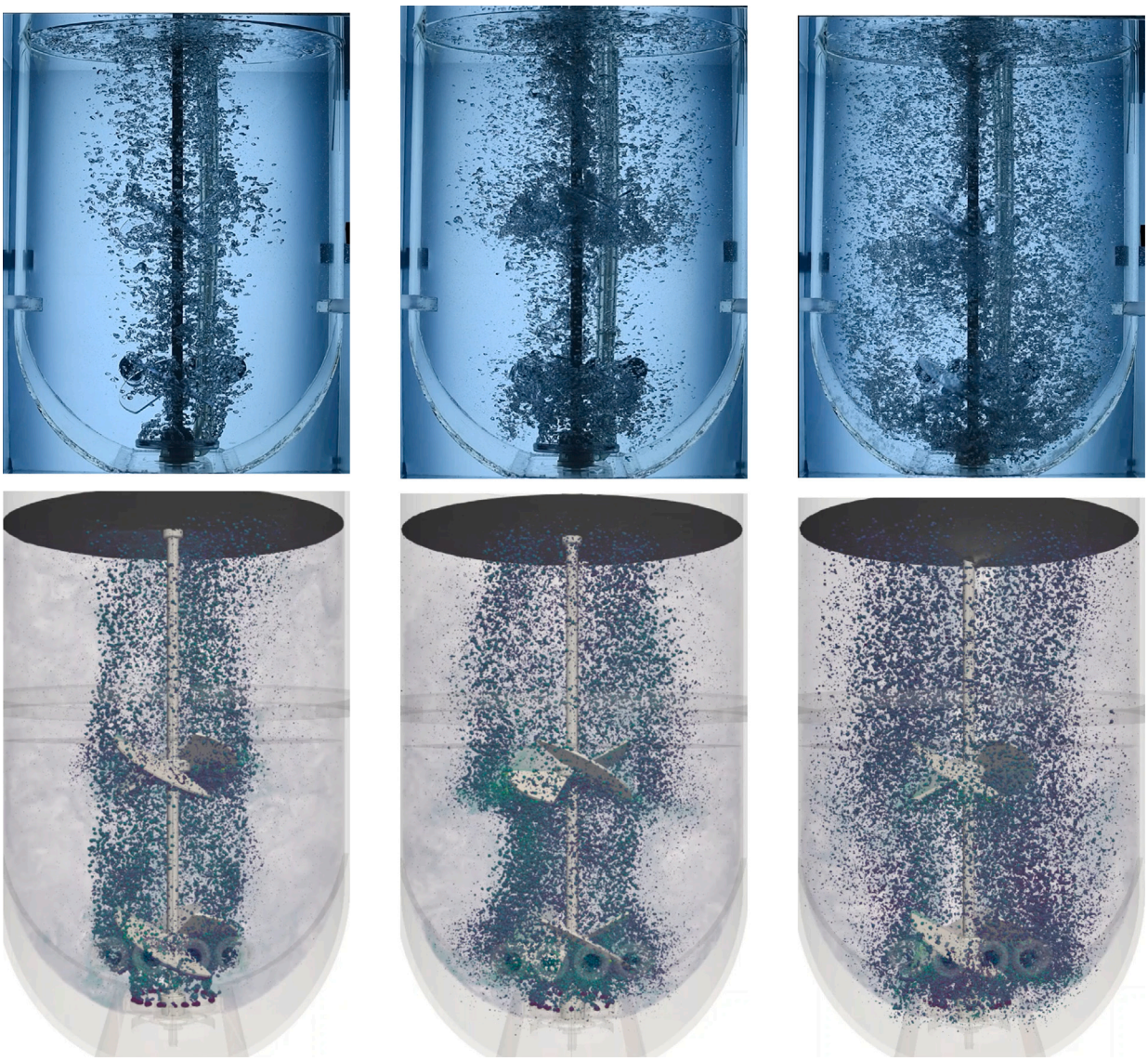

Fig. 6. Snapshots from the experiments (top row) and the simulations utilising the TBBM (bottom row) for an aeration rate of $\dot{V}_G = 20\,\mathrm{L\,min^{-1}}$ and a stirrer frequency of $n = 50\,\mathrm{rpm}$ (left), $n = 100\,\mathrm{rpm}$ (middle), and $n = 150\,\mathrm{rpm}$ (right).

second this yields a total wall time of ca. 15 to 60 min to come up with a statistically converged bubble size distribution utilising the TBBM for this 200 L vessel using two NVIDIA H100 Tensor-Core GPUs. Utilising the model proposed by Kawase and Moo-Young on the other hand, took between six and ten minutes wall time for one simulated second, leading to a slightly higher but overall comparably similar necessary wall time to retrieve a statistically converged BSD.

The BSD obtained with the TBBM almost matches the experimental BSD for the smallest stirrer frequency of $n = 50\,\mathrm{rpm}$, while over-predicting the amount of small bubbles slightly in the case of the stirrer frequencies $n = 100\,\mathrm{rpm}$ and $n = 150\,\mathrm{rpm}$. However, this might also be caused by errors due to the image analysis from the experimental results. The model of Kawase and Moo-Young on the other hand, underpredicts the amount of small bubbles clearly for the stirrer frequencies $n = 50\,\mathrm{rpm}$ and $150\,\mathrm{rpm}$ and shows a good match with both, the experimental data and the data achieved with the TBBM for the stirrer frequency $n = 100\,\mathrm{rpm}$. Further, the model of Kawase and Moo Young overpredicts the amount of those bubbles with a diameter of $d_{\mathrm{initial}} = 0.01\,\mathrm{m}$. It seems that utilising this model, the initial bubble diameter has a significant influence on the final BSD results, leading to a bimodal distribution. This behaviour is not visible utilising the new TBBM proposed here. The TBBM performs particularly well over the full range of the observed process conditions and is robust against varying initial bubble sizes, compare Fig. 10 in Appendix C. Thus, further improvement is possible but overall the experimental BSDs are mirrored well.

4. Conclusions and outlook

A Trajectory-Based Breakup Model (TBBM) was developed and implemented to describe the breakup of gaseous bubbles in a background flow based on first principles. In the TBBM, each bubble is observed along its respective trajectory individually and modelled as a Kelvin–Voigt element. These bubbles remain individual throughout their respective lifetime and no clustering is implemented. Hereby, the outer acting force is calculated by taking into account the stretch of the fluid surrounding each individual bubble retrieved from the rate-of-strain tensor. According to the contour plot of the largest eigenvalue

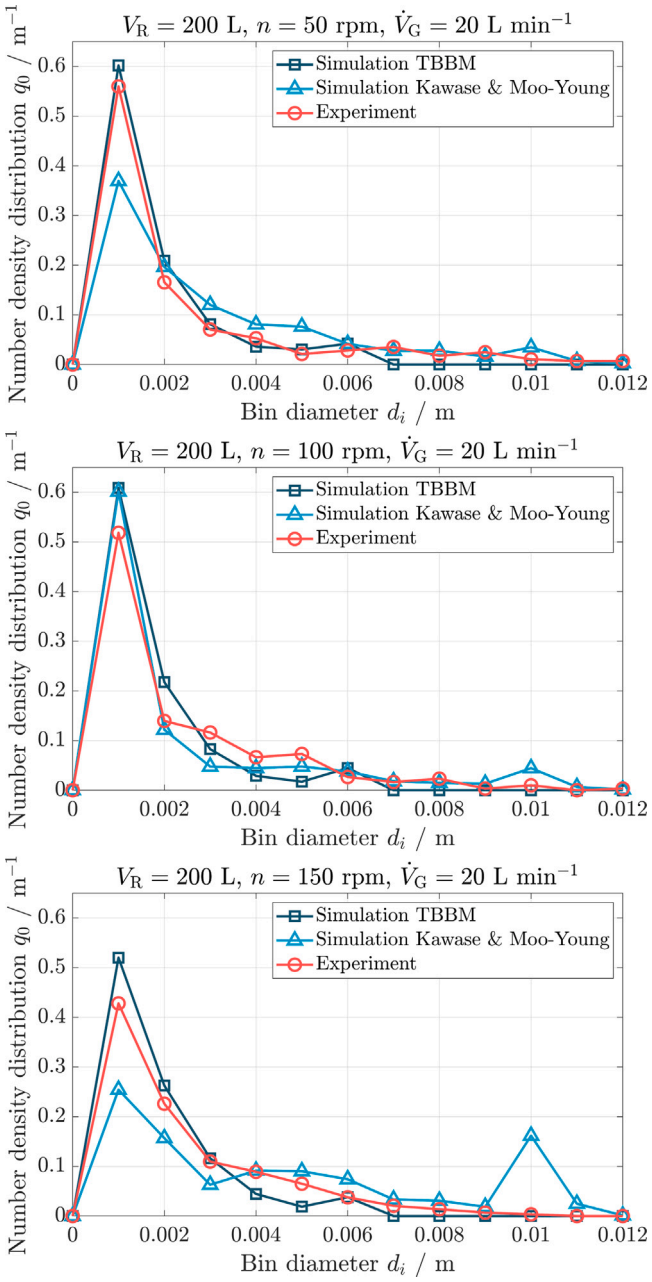

Fig. 7. Bubble size distributions for an aeration rate of $\dot{V}_G = 20\,\mathrm{L\,min^{-1}}$ and a stirrer frequency of $n = 50$ rpm (top), $n = 100$ rpm (middle), and $n = 150$ rpm (bottom) for the experiments, the simulations with the developed TBBM model, and the model proposed by Kawase and Moo-Young.

of the CGST, compare Fig. 9 in Appendix B, the largest stretch and, thus the regions of most probable breakup can be found beneath the stirrers. In the current version of the TBBM the breakup is restricted to two daughter bubbles, which could be a source for errors, since many processes exist in which three or more daughter bubbles result from a breakup event. Nevertheless, this error is assumed to not be large since a recently broken bubble can break again after some time if the new deformation is high enough. The forces mirroring the effects of the spring and the damper are described by the interfacial tension and viscous effects, respectively.

The proposed model works well for an aerated replica of the BIOSTAT STR® 200 from Sartorius Stedim Biotech GmbH with two segment stirrers and filled with DI water and PBS. The retrieved bubble size distributions match the ones obtained experimentally qualitatively and quantitatively. For larger stirrer frequencies the small sized bubbles might be slightly overpredicted due to some modelling assumptions. For the outer acting force, only the direction of the largest stretch was taken into account assuming that the bubble instantaneously redirects its major axis in the same direction. The rotation induced by the interaction of fluid and bubble and an associated possible change of the eigendirection of the bubble have not been taken into account so far. Hence, the assumed stretch may not fully reflect the real stretch that the bubble experiences during a specific interval of time, but is a supremum of all the possible stretches at a specific point in space during one numerical time step. Due to the small time intervals with regard to the numerical simulation, this source of error is assumed to not be very significant. Another source for mismatch might be the experimental evaluation which was achieved optically. Since in the experiments bubbles shade objects behind them, smaller bubbles could be missed which are, however, accounted for in the simulations, since here each and every bubble is taken into account, independently whether it is behind a larger bubble or not. Further, in this study only the breakup was modelled using the newly developed TBBM. The bubble coalescence on the other hand was not modelled with a self-developed model, but with the M-Star default model [82] based on a critical Reynolds number [83].

For future work, the TBBM will be applied to and validated with other scales with varying volumes from 3 L to 15000 L and other types of reactors, such as the Jet Loop Reactor, available at the IMS. Further, the medium will be changed to test whether the model still predicts BSDs well for completely different physical properties of the fluids, e.g. solvents or mixtures of solvents with reactive gases, and further for flow regimes in which strictly non-ellipsoidal bubbles are to be expected. The physical properties, like viscosities or interfacial tension, of such systems will be determined by thermodynamic software packages such as FeO_S [84]. For model improvement, the rotation and the eigendirections of the bubble can also be taken into account, leading to a better estimation of the actual bubble deformation, hence to a more accurate prediction of the breakup, which is slightly overestimated in the current state of the model. A more precise or flexible breakup criterion, taking into account the local slip velocity and the actual bubble's deformation, can be formulated. With this, a more precise expression for the drag force will be considered [85,86], which will take even further into account the local phenomena along the bubbles' trajectories and, thus improve the prediction of the BSD. Further, the modelling of oblate ellipsoids has not yet been treated and is the topic of the next step in the model improvement, potentially leading to a better prediction of the deformation in regions where the bubbles rise freely without a strong influence of the stirrer. The estimation of the Basset history term for randomly chosen bubbles from the moment of their respective initialisation to one second of their rise have shown mean values of approximately 26 % of the buoyancy force, which is in a reasonable range, compared to Muniz and Sommerfeld [87]. In future calculations, this term will be implemented for a more precise prediction of the bubbles' positions [88] and, thus a more precise prediction of the local deformation and breakup which should be important especially close to moving walls, like stirrer blades, where comparably high slip velocities and slip accelerations are expected. To enable the implementation with acceptable computational costs, a recently developed fast algorithm for the estimation of the Basset history term from collaborators in the CRC 1615 will be used [89,90]. However, the comparison of experimental and numerical results in Figs. 6 and 7 shows that even with the simplifications and assumptions an acceptable accuracy is already reached. In the farther future, a model concerning the mass transfer coefficient based on the degree of the bubble deformation is to be formulated and the extension to non-Newtonian fluids will be carried out. Altogether, the new TBBM model offers a huge variety of possibilities to determine more precise BSDs for different applications within a reasonable amount of computational effort. The new approach will be an important pillar for the development of digital twins for SMART reactors in the research of the CRC 1615 "SMART Reactors".

CRediT authorship contribution statement

Christian Weiland: Writing – original draft, Visualization, Software, Methodology, Investigation, Formal analysis, Conceptualization. **Alexandra von Kameke:** Writing – review & editing, Methodology, Formal analysis, Conceptualization. **Michael Schlüter:** Writing – review & editing, Supervision, Resources, Methodology, Funding acquisition, Conceptualization.

Declaration of competing interest

The authors declare that they have no known competing financial interests or personal relationships that could have appeared to influence the work reported in this paper.

Data availability

Data will be made available on request.

Acknowledgements

This project is funded by the Deutsche Forschungsgemeinschaft (DFG, German Research Foundation) – SFB 1615 – 503850735.

The authors thank Daniele Marchisio for the pleasant and encouraging conversation during the Jahrestreffen 2024 der DECHEMA/VDI Fachgruppen Mehrphasenströmungen (MPH), Computational Fluid Dynamics (CFD) und Aerosoltechnik (AT) in Bremen, Germany.

The authors thank Johannes Wutz from M-Star Simulations, LCC. for the discussions regarding setting up the User Defined Functions in M-Star CFD.

The authors thank Vincent Bernemann and Sartorius Stedim Biotech GmbH for the help creating the geometry file and for providing the experimental data.

The authors thank Jürgen Fitschen and Boehringer Ingelheim Pharma GmbH & Co. KG for providing the geometry and data for further internal validation.

The authors thank Marc Maly for proofreading.

Appendix A. Mesh study

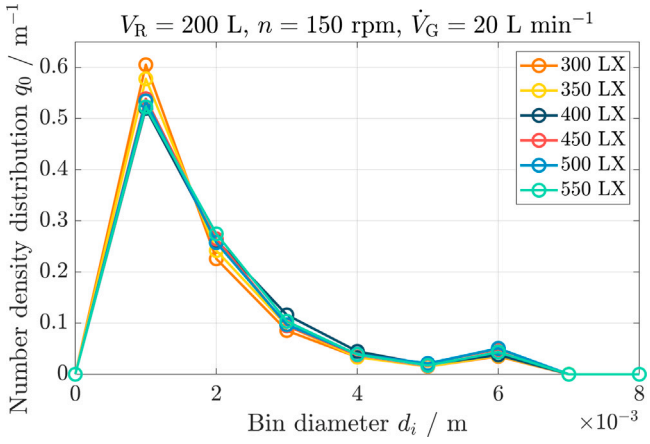

Fig. 8. Mesh study for a different number of lattice points along the x-axis, BSDs evaluated in the red box in Fig. 5.

Appendix B. Eigenvalue λ_3 field

Fig. 9. Contour of the largest eigenvalue λ_3 of the CGST for the case $n = 150$ rpm on the x-plane.

Appendix C. Initial bubble diameter

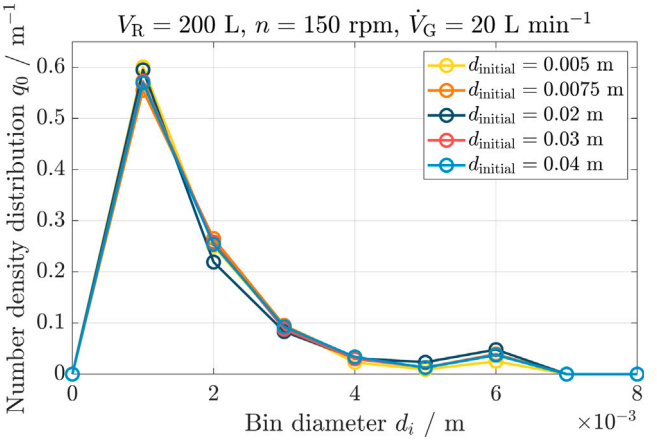

Fig. 10. Influence of the initial bubble size, BSDs evaluated in the red box in Fig. 5.

Appendix D. Trajectories

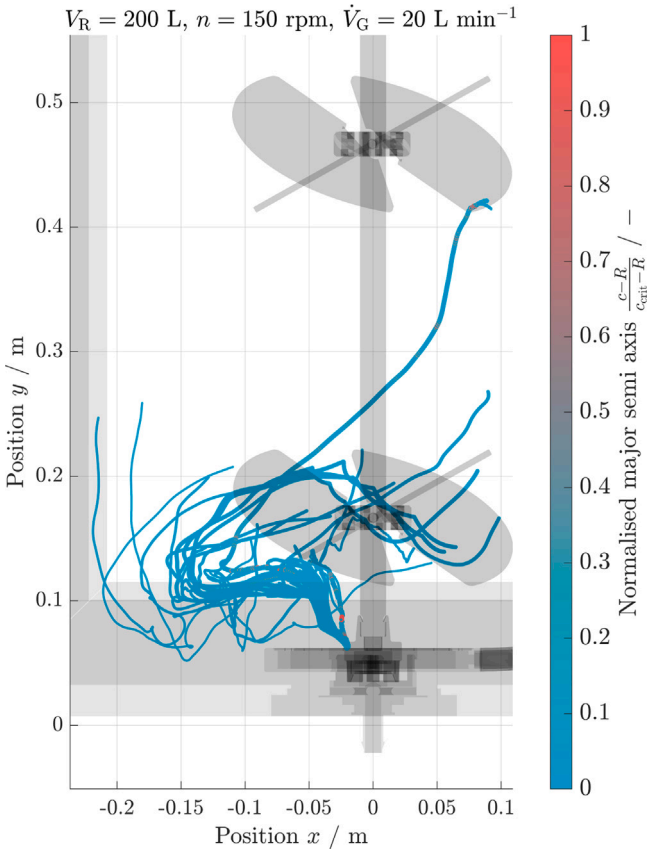

Fig. 11. Trajectories of two bubbles initiated at the sparger and all their children over the time of one second, the widths of the lines correspond qualitatively to the bubble's sizes.

Appendix E. Code for the estimation of the largest eigenvalue

```
// Define  eigenvector entries and tolerance
int k;
int maxk = 400;

float EVX;
float EVY;
float EVZ;

// Initial guess for the eigenvector
float EVX_old = 1.0;
float EVY_old = 1.0;
float EVZ_old = 1.0;
float error=0.001;
float lambda_old = -20.0;
float lambda_new;
lambda = -10.0;

// Define Jacobian entries
float JXX = 1.0+Lxx*dt;
float JXY = Lxy*dt;
float JXZ = Lxz*dt;
float JYX = Lyx*dt;
float JYY = 1.0+Lyy*dt;
float JYZ = Lyz*dt;
float JZX = Lzx*dt;
float JZY = Lzy*dt;
float JZZ = 1.0+Lzz*dt;


// Define entries of JF'JF
float JTXX = JXX*JXX + JYX*JYX + JZX*JZX;
float JTXY = JXX*JXY + JYX*JYY + JZX*JZY;
float JTXZ = JXX*JXZ + JYX*JYZ + JZX*JZZ;

float JTYX = JXY*JXX + JYY*JYX + JZY*JZX;
float JTYY = JXY*JXY + JYY*JYY + JZY*JZY;
float JTYZ = JXY*JXZ + JYY*JYZ + JZY*JZZ;

float JTZX = JXZ*JXX + JYZ*JYX + JZZ*JZX;
float JTZY = JXZ*JXY + JYZ*JYY + JZZ*JZY;
float JTZZ = JXZ*JXZ + JYZ*JYZ + JZZ*JZZ;

// Power method
for(k=1; k<maxk; k++){
EVX = JTXX*EVX_old + JTXY*EVY_old + JTXZ*EVZ_old;
EVY = JTYX*EVX_old + JTYY*EVY_old + JTYZ*EVZ_old;
EVZ = JTZX*EVX_old + JTZY*EVY_old + JTZZ*EVZ_old;

lambda_new = ( EVX*(EVX*JTXX + EVY*JTYX + EVZ*JTZX)
 + EVY*(EVX*JTXY + EVY*JTYY + EVZ*JTZY)
 + EVZ*(EVX*JTXZ + EVY*JTYZ + EVZ*JTZZ) )
 / (EVX*EVX + EVY*EVY + EVZ*EVZ);
if(fabsf(lambda_old - lambda_new) < error){
   lambda = lambda_new;
   if(lambda<1.0) //lambda cannot be smaller than 1
   lambda=1.0;

   k=maxk;
}else{
   lambda_old = lambda_new;
   EVX_old = EVX;
   EVY_old = EVY;
   EVZ_old = EVZ;
}
}

if(lambda<1)
  lambda=1;
```

Appendix F. Code for the estimation of the major semi axis

```
float sigma = 0.069; // N/m
float etaF = 0.00079; // Pa s,
 dynamic viscosity of continuous phase
float etaB = 0.0000172; // Pa s,
 dynamic viscosity of bubbles
float radius = d_p/2.0;
float a; // minor principle axis;

if(tsb_p < 3.0*dt)
majorC_p = radius;

a = sqrtf(powf(radius,3.0)/majorC_p);

if(tsb_p >= 3.0*dt) //short regeneration time
 to prevent cascading effect
majorC_p = majorC_p + radius * etaF/etaB
 * (sqrtf(lambda)-1.0)/2.0 - sigma/2.0/a/etaB
 * ( majorC_p - radius ) * dt;

if(majorC_p < radius)
majorC_p = radius;
```

Appendix G. Code for the bubble breakup and the daughter size

```
float radius = d_p/2.0;
float rhoP = 1.204;
float rhoF = 998.2;
float pi = 3.1415926;
float S_E = 2.0 * pi * sqrtf(powf(radius,3.0)/majorC_p)
 * (sqrtf(powf(radius,3.0)/majorC_p)
 + powf(majorC_p,2.0)/sqrtf(majorC_p * majorC_p
 - powf(radius,3.0)/majorC_p) * asinf(sqrtf( majorC_p
 * majorC_p - powf(radius,3.0)/majorC_p )/majorC_p));
float fv_run=0.0;
float g = 9.81;
float sigma = 0.069;
float S;
float dS = 1000.0;
float dS_neu;
float nuF = 7.9e-07;
float lKolmogorov = powf(powf(nuF,3.0)/e, 1.0/4.0);
float a = sqrt(powf(radius,3.0)/majorC_p);

if(vol_p * (rhoF - rhoP) * g > 2*a * pi
    * sigma && 2*majorC_p > lKolmogorov){
  doBreakup = true;
  while(fv_run <= 0.5) {
    S = pi * d_p * d_p * (powf(fv_run,2/3)
      + powf(1-fv_run,2/3));
    dS_neu = fabsf(S_E - S);
    if(dS_neu < dS){
      dS = dS_neu;
      fv = fv_run;
    }
    fv_run = fv_run + 0.01;
  }
}
else{
  doBreakup = false;
}
```

References

[1] Y. Liao, D. Lucas, A literature review of theoretical models for drop and bubble breakup in turbulent dispersions, Chem. Eng. Sci. 64 (15) (2009) 3389–3406, http://dx.doi.org/10.1016/j.ces.2009.04.026, URL https://linkinghub.elsevier.com/retrieve/pii/S0009250909002759.

[2] Y. Liao, D. Lucas, A literature review on mechanisms and models for the coalescence process of fluid particles, Chem. Eng. Sci. 65 (10) (2010) 2851–2864, http://dx.doi.org/10.1016/j.ces.2010.02.020, URL https://linkinghub.elsevier.com/retrieve/pii/S000925091000093X.

[3] H. Hulburt, S. Katz, Some problems in particle technology, Chem. Eng. Sci. 19 (8) (1964) 555–574, http://dx.doi.org/10.1016/0009-2509(64)85047-8, URL https://linkinghub.elsevier.com/retrieve/pii/0009250964850478.

[4] D. Ramkrishna, Population Balances: Theory and Applications to Particulate Systems in Engineering, Academic Press, San Diego, CA, 2000.

[5] D. L. Marchisio, R. Dennis Vigil, R. O. Fox, Implementation of the quadrature method of moments in CFD codes for aggregation–breakage problems, Chem. Eng. Sci. 58 (15) (2003) 3337–3351, http://dx.doi.org/10.1016/S0009-2509(03)00211-2, URL https://linkinghub.elsevier.com/retrieve/pii/S0009250903002112.

[6] D.L. Marchisio, M. Soos, J. Sefcik, M. Morbidelli, Role of turbulent shear rate distribution in aggregation and breakage processes, AIChE J. 52 (1) (2006) 158–173, http://dx.doi.org/10.1002/aic.10614, URL https://aiche.onlinelibrary.wiley.com/doi/10.1002/aic.10614.

[7] J. Sanyal, D.L. Marchisio, R.O. Fox, K. Dhanasekharan, On the comparison between population balance models for CFD simulation of bubble columns, Ind. Eng. Chem. Res. 44 (14) (2005) 5063–5072, http://dx.doi.org/10.1021/ie049555j, URL https://pubs.acs.org/doi/10.1021/ie049555j.

[8] E. Gavi, D.L. Marchisio, A.A. Barresi, M.G. Olsen, R.O. Fox, Turbulent precipitation in micromixers: CFD simulation and flow field validation, Chem. Eng. Res. Des. 88 (9) (2010) 1182–1193, http://dx.doi.org/10.1016/j.cherd.2010.01.025, URL https://linkinghub.elsevier.com/retrieve/pii/S0263876210000390.

[9] S. Maaß, M. Kraume, Determination of breakage rates using single drop experiments, Chem. Eng. Sci. 70 (2012) 146–164, http://dx.doi.org/10.1016/j.ces.2011.08.027, URL https://linkinghub.elsevier.com/retrieve/pii/S0009250911005963.

[10] S. Maaß, A. Gäbler, A. Zaccone, A. Paschedag, M. Kraume, Experimental investigations and modelling of breakage phenomena in stirred liquid/liquid systems, Chem. Eng. Res. Des. 85 (5) (2007) 703–709, http://dx.doi.org/10.1205/cherd06187, URL https://linkinghub.elsevier.com/retrieve/pii/S0263876207731015.

[11] A. Buffo, M. Jama, V. Alopaeus, Liquid–liquid extraction in a rotating disc column: Solution of 2D population balance with HMMC, Chem. Eng. Res. Des. 115 (2016) 270–281, http://dx.doi.org/10.1016/j.cherd.2016.09.002, URL https://linkinghub.elsevier.com/retrieve/pii/S0263876216302878.

[12] A. Buffo, V. Alopaeus, Solution of bivariate population balance equations with high-order moment-conserving method of classes, Comput. Chem. Eng. 87 (2016) 111–124, http://dx.doi.org/10.1016/j.compchemeng.2015.12.013, URL https://linkinghub.elsevier.com/retrieve/pii/S0098135415003774.

[13] W. Zhao, M.A. Jama, A. Buffo, V. Alopaeus, Population balance model and experimental validation for reactive dissolution of particle agglomerates, Comput. Chem. Eng. 108 (2018) 240–249, http://dx.doi.org/10.1016/j.compchemeng.2017.09.019, URL https://linkinghub.elsevier.com/retrieve/pii/S0098135417303381.

[14] G.I. Taylor, Statistical theory of turbulenc, Proc. R. Soc. Lond. Ser. A - Math. Phys. Sci. 151 (873) (1935) 421–444, http://dx.doi.org/10.1098/rspa.1935.0158, URL https://royalsocietypublishing.org/doi/10.1098/rspa.1935.0158.

[15] J.O. Hinze, Fundamentals of the hydrodynamic mechanism of splitting in dispersion processes, AIChE J. 1 (3) (1955) 289–295, http://dx.doi.org/10.1002/aic.690010303, URL https://aiche.onlinelibrary.wiley.com/doi/10.1002/aic.690010303.

[16] G.K. Batchelor, Pressure fluctuations in isotropic turbulence, Math. Proc. Cambridge Philos. Soc. 47 (2) (1951) 359–374, http://dx.doi.org/10.1017/S0305004100026712.

[17] Y. Kawase, M. Moo-Young, Mathematical models for design of bioreactors: Applications of: Kolmogoroff's theory of isotropic turbulence, Chem. Eng. J. 43 (1) (1990) B19–B41, http://dx.doi.org/10.1016/0300-9467(90)80048-H, URL https://www.sciencedirect.com/science/article/pii/030094679080048H.

[18] C. Martínez-Bazán, J.L. Montañés, J.C. Lasheras, On the breakup of an air bubble injected into a fully developed turbulent flow. Part 1. Breakup frequency, J. Fluid Mech. 401 (1999) 157–182, http://dx.doi.org/10.1017/S0022112099006680, URL https://www.cambridge.org/core/product/identifier/S0022112099006680/type/journal_article.

[19] C. Martínez-Bazán, J.L. Montañés, J.C. Lasheras, On the breakup of an air bubble injected into a fully developed turbulent flow. Part 2. Size PDF of the resulting daughter bubbles, J. Fluid Mech. 401 (1999) 183–207, http://dx.doi.org/10.1017/S0022112099006692, URL https://www.cambridge.org/core/product/identifier/S0022112099006692/type/journal_article.

[20] M.J. Prince, H.W. Blanch, Bubble coalescence and break-up in air-sparged bubble columns, AIChE J. 36 (10) (1990) 1485–1499, http://dx.doi.org/10.1002/aic.690361004, URL https://aiche.onlinelibrary.wiley.com/doi/abs/10.1002/aic.690361004.

[21] H. Luo, H.F. Svendsen, Theoretical model for drop and bubble breakup in turbulent dispersions, AIChE J. 42 (5) (1996) 1225–1233, http://dx.doi.org/10.1002/aic.690420505, URL https://aiche.onlinelibrary.wiley.com/doi/10.1002/aic.690420505.

[22] F. Lehr, M. Millies, D. Mewes, Bubble-size distributions and flow fields in bubble columns, AIChE J. 48 (11) (2002) 2426–2443, http://dx.doi.org/10.1002/aic.690481103, URL https://aiche.onlinelibrary.wiley.com/doi/abs/10.1002/aic.690481103.

[23] C. Xing, T. Wang, K. Guo, J. Wang, A unified theoretical model for breakup of bubbles and droplets in turbulent flows, AIChE J. 61 (4) (2015) 1391–1403, http://dx.doi.org/10.1002/aic.14709, URL https://aiche.onlinelibrary.wiley.com/doi/10.1002/aic.14709.

[24] E.I.V. Van Den Hengel, N.G. Deen, J.A.M. Kuipers, Application of coalescence and breakup models in a discrete bubble model for bubble columns, Ind. Eng. Chem. Res. 44 (14) (2005) 5233–5245, http://dx.doi.org/10.1021/ie0492449, URL https://pubs.acs.org/doi/10.1021/ie0492449.

[25] Y. Lau, W. Bai, N. Deen, J. Kuipers, Numerical study of bubble break-up in bubbly flows using a deterministic Euler–Lagrange framework, Chem. Eng. Sci. 108 (2014) 9–22, http://dx.doi.org/10.1016/j.ces.2013.12.034, URL https://linkinghub.elsevier.com/retrieve/pii/S0009250913008294.

[26] D. Jain, J.A.M. Kuipers, N.G. Deen, Numerical study of coalescence and breakup in a bubble column using a hybrid volume of fluid and discrete bubble model approach, Chem. Eng. Sci. 119 (2014) 134–146, http://dx.doi.org/10.1016/j.ces.2014.08.026, URL https://www.sciencedirect.com/science/article/pii/S0009250914004448.

[27] Y. Mast, R. Takors, Transferring bubble breakage models tailored for Euler-Euler approaches to Euler-Lagrange simulations, Processes 11 (4) (2023) 1018, http://dx.doi.org/10.3390/pr11041018, URL https://www.mdpi.com/2227-9717/11/4/1018.

[28] C. Coulaloglou, L. Tavlarides, Description of interaction processes in agitated liquid-liquid dispersions, Chem. Eng. Sci. 32 (11) (1977) 1289–1297, http://dx.doi.org/10.1016/0009-2509(77)85023-9, URL https://linkinghub.elsevier.com/retrieve/pii/0009250977850239.

[29] P.M. Wilkinson, A. Van Schayk, J.P. Spronken, L.L. Van Dierendonck, The influence of gas density and liquid properties on bubble breakup, Chem. Eng. Sci. 48 (7) (1993) 1213–1226, http://dx.doi.org/10.1016/0009-2509(93)81003-E, URL https://linkinghub.elsevier.com/retrieve/pii/000925099381003E.

[30] H. Zhang, Y. Wang, A. Sayyar, T. Wang, Experimental study on breakup of a single bubble in a stirred tank: Effect of gas density and liquid properties, AIChE J. 69 (1) (2023) e17511, http://dx.doi.org/10.1002/aic.17511, URL https://aiche.onlinelibrary.wiley.com/doi/10.1002/aic.17511.

[31] G. Zhou, S.M. Kresta, Correlation of mean drop size and minimum drop size with the turbulence energy dissipation and the flow in an agitated tank, Chem. Eng. Sci. 53 (11) (1998) 2063–2079, http://dx.doi.org/10.1016/S0009-2509(97)00438-7, URL https://linkinghub.elsevier.com/retrieve/pii/S0009250997004387.

[32] M. Martín, F.J. Montes, M.A. Galán, Influence of impeller type on the bubble breakup process in stirred tanks, Ind. Eng. Chem. Res. 47 (16) (2008) 6251–6263, http://dx.doi.org/10.1021/ie800063v, URL https://pubs.acs.org/doi/10.1021/ie800063v.

[33] S. Alves, C. Maia, J. Vasconcelos, A. Serralheiro, Bubble size in aerated stirred tanks, Chem. Eng. J. 89 (1–3) (2002) 109–117, http://dx.doi.org/10.1016/S1385-8947(02)00008-6, URL https://linkinghub.elsevier.com/retrieve/pii/S1385894702000086.

[34] R. Parthasarathy, N. Ahmed, Bubble size distribution in a gas sparged vessel agitated by a rushton turbine, Ind. Eng. Chem. Res. 33 (3) (1994) 703–711, http://dx.doi.org/10.1021/ie00027a032, URL https://pubs.acs.org/doi/abs/10.1021/ie00027a032.

[35] C. Tsouris, L.L. Tavlarides, Breakage and coalescence models for drops in turbulent dispersions, AIChE J. 40 (3) (1994) 395–406, http://dx.doi.org/10.1002/aic.690400303, URL https://aiche.onlinelibrary.wiley.com/doi/10.1002/aic.690400303.

[36] A. Sarimeseli, G. Kelbaliyev, Modeling of the break-up of deformable particles in developed turbulent flow, Chem. Eng. Sci. 59 (6) (2004) 1233–1240, http://dx.doi.org/10.1016/j.ces.2003.09.047, URL https://linkinghub.elsevier.com/retrieve/pii/S000925090400017X.

[37] M. Baltussen, Bubbles on the Cutting Edge : Direct Numerical Simulations of Gas-Liquid-Solid Three-Phase Flows (Ph.D. thesis), Technische Universiteit Eindhoven, Chemical Engineering and Chemistry, 2015, Proefschrift.

[38] S. Nachtigall, D. Zedel, M. Kraume, Analysis of drop deformation dynamics in turbulent flow, Chin. J. Chem. Eng. 24 (2) (2016) 264–277, http://dx.doi.org/10.1016/j.cjche.2015.06.003, URL https://linkinghub.elsevier.com/retrieve/pii/S1004954115002098.

[39] F. Risso, J. Fabre, Oscillations and breakup of a bubble immersed in a turbulent field, J. Fluid Mech. 372 (1998) 323–355, http://dx.doi.org/10.1017/S0022112098002705, URL https://www.cambridge.org/core/product/identifier/S0022112098002705/type/journal_article.

[40] B. Lalanne, O. Masbernat, F. Risso, A model for drop and bubble breakup frequency based on turbulence spectra, AIChE J. 65 (1) (2019) 347–359, http://dx.doi.org/10.1002/aic.16374, URL https://aiche.onlinelibrary.wiley.com/doi/10.1002/aic.16374.

[41] A. Vela-Martín, M. Avila, Deformation of drops by outer eddies in turbulence, J. Fluid Mech. 929 (2021) A38, http://dx.doi.org/10.1017/jfm.2021.879, URL https://www.cambridge.org/core/product/identifier/S002211202100879X/type/journal_article.

[42] Y. Qi, A.U. Mohammad Masuk, R. Ni, Towards a model of bubble breakup in turbulence through experimental constraints, Int. J. Multiph. Flow 132 (2020) 103397, http://dx.doi.org/10.1016/j.ijmultiphaseflow.2020.103397, URL https://linkinghub.elsevier.com/retrieve/pii/S0301932220305061.

[43] Y. Qi, S. Tan, N. Corbitt, C. Urbanik, A.K.R. Salibindla, R. Ni, Fragmentation in turbulence by small eddies, Nature Commun. 13 (1) (2022) 469, http://dx.doi.org/10.1038/s41467-022-28092-3, URL https://www.nature.com/articles/s41467-022-28092-3.

[44] R. Ni, S. Kramel, N.T. Ouellette, G.A. Voth, Measurements of the coupling between the tumbling of rods and the velocity gradient tensor in turbulence, J. Fluid Mech. 766 (2015) 202–225, http://dx.doi.org/10.1017/jfm.2015.16, URL https://www.cambridge.org/core/product/identifier/S0022112015000166/type/journal_article.

[45] R. Ni, Deformation and breakup of bubbles and drops in turbulence, Annu. Rev. Fluid Mech. 56 (1) (2024) 319–347, http://dx.doi.org/10.1146/annurev-fluid-121021-034541, URL https://www.annualreviews.org/doi/10.1146/annurev-fluid-121021-034541.

[46] P. Maffettone, M. Minale, Equation of change for ellipsoidal drops in viscous flow, J. Non-Newton. Fluid Mech. 78 (2–3) (1998) 227–241, http://dx.doi.org/10.1016/S0377-0257(98)00065-2, URL https://linkinghub.elsevier.com/retrieve/pii/S0377025798000652.

[47] A.U.M. Masuk, A.K.R. Salibindla, R. Ni, Simultaneous measurements of deforming Hinze-scale bubbles with surrounding turbulence, J. Fluid Mech. 910 (2021) A21, http://dx.doi.org/10.1017/jfm.2020.933, URL https://www.cambridge.org/core/product/identifier/S0022112020009337/type/journal_article.

[48] A.U.M. Masuk, Y. Qi, A.K. Salibindla, R. Ni, Towards a phenomenological model on the deformation and orientation dynamics of finite-sized bubbles in both quiescent and turbulent media, J. Fluid Mech. 920 (2021) A4, http://dx.doi.org/10.1017/jfm.2021.390, URL https://www.cambridge.org/core/product/identifier/S0022112021003906/type/journal_article.

[49] L. Vobecká, S. Orvalho, M. Zedníková, J. Vejražka, J. Tihon, Damping effect of surfactants on induced bubble shape deformations, Phys. Fluids 35 (12) (2023) 122120, http://dx.doi.org/10.1063/5.0174954, URL https://pubs.aip.org/pof/article/35/12/122120/2930608/Damping-effect-of-surfactants-on-induced-bubble.

[50] J. Vejražka, M. Zedníková, P. Stanovský, Experiments on breakup of bubbles in a turbulent flow, AIChE J. 64 (2) (2018) 740–757, http://dx.doi.org/10.1002/aic.15935, URL https://aiche.onlinelibrary.wiley.com/doi/10.1002/aic.15935.

[51] W. Thomson, IV. on the elasticity and viscosity of metals, Proc. R. Soc. Lond. 14 (1865) 289–297, http://dx.doi.org/10.1098/rspl.1865.0052, URL https://royalsocietypublishing.org/doi/10.1098/rspl.1865.0052.

[52] W. Voigt, Ueber innere Reibung fester Körper, insbesondere der Metalle, Ann. Phys., Lpz. 283 (12) (1892) 671–693, http://dx.doi.org/10.1002/andp.18922831210, URL https://onlinelibrary.wiley.com/doi/10.1002/andp.18922831210.

[53] J.S. Lagisetty, P.K. Das, R. Kumar, K.S. Gandhi, Breakage of viscous and non-Newtonian drops in stirred dispersions, Chem. Eng. Sci. 41 (1) (1986) 65–72, http://dx.doi.org/10.1016/0009-2509(86)85198-3, URL https://www.sciencedirect.com/science/article/pii/0009250986851983.

[54] D.K.R. Nambiar, R. Kumar, T.R. Das, K.S. Gandhi, A new model for the breakage frequency of drops in turbulent stirred dispersions, Chem. Eng. Sci. 47 (12) (1992) 2989–3002, http://dx.doi.org/10.1016/0009-2509(92)87001-7, URL https://www.sciencedirect.com/science/article/pii/0009250992870017.

[55] G. Haller, G. Yuan, Lagrangian coherent structures and mixing in two-dimensional turbulence, Physica D 147 (3–4) (2000) 352–370, http://dx.doi.org/10.1016/S0167-2789(00)00142-1, URL https://linkinghub.elsevier.com/retrieve/pii/S0167278900001421.

[56] G. Haller, Distinguished material surfaces and coherent structures in three-dimensional fluid flows, Physica D 149 (4) (2001) 248–277, http://dx.doi.org/10.1016/S0167-2789(00)00199-8, URL https://linkinghub.elsevier.com/retrieve/pii/S0167278900001998.

[57] A. von Kameke, S. Kastens, S. Rüttinger, S. Herres-Pawlis, M. Schlüter, How coherent structures dominate the residence time in a bubble wake: an experimental example, 2019, URL http://arxiv.org/abs/1901.07081, arXiv:1901.07081 [physics].

[58] C.G. Llamas, C. Spille, S. Kastens, D.G. Paz, M. Schlüter, A. Kameke, Potential of Lagrangian analysis methods in the study of chemical reactors, Chem. Ing. Tech. 92 (5) (2020) 540–553, http://dx.doi.org/10.1002/cite.201900147, URL https://onlinelibrary.wiley.com/doi/10.1002/cite.201900147.

[59] L. Kursula, F. Kexel, J. Fitschen, M. Hoffmann, M. Schlüter, A. Von Kameke, Unsteady mass transfer in bubble wakes analyzed by Lagrangian coherent structures in a flat-bed reactor, Processes 10 (12) (2022) 2686, http://dx.doi.org/10.3390/pr10122686, URL https://www.mdpi.com/2227-9717/10/12/2686.

[60] C. Weiland, E. Steuwe, J. Fitschen, M. Hoffmann, M. Schlüter, K. Padberg-Gehle, A. von Kameke, Computational study of three-dimensional Lagrangian transport and mixing in a stirred tank reactor, Chem. Eng. J. Adv. 14 (2023) 100448, http://dx.doi.org/10.1016/j.ceja.2023.100448, URL https://linkinghub.elsevier.com/retrieve/pii/S2666821123000066.

[61] R. Clift, J.R. Grace, M.E. Weber, Bubbles, Drops, and Particles, third print, Acad. Press, New York, NY, 1992.

[62] J.A. Thomas, B. DeVincentis, J. Wutz, F. Ricci, Predicting the diameters of droplets produced in turbulent liquid–liquid dispersion, AIChE J. 68 (7) (2022) e17667, http://dx.doi.org/10.1002/aic.17667, URL https://aiche.onlinelibrary.wiley.com/doi/10.1002/aic.17667.

[63] P.G. Saffman, The lift on a small sphere in a slow shear flow, J. Fluid Mech. 22 (2) (1965) 385–400, http://dx.doi.org/10.1017/S0022112065000824, URL https://www.cambridge.org/core/product/identifier/S0022112065000824/type/journal_article.

[64] C.T. Crowe, J.D. Schwarzkopf, M. Sommerfeld, Y. Tsuji, Multiphase Flows with Droplets and Particles, second ed., CRC Press, 2011, http://dx.doi.org/10.1201/b11103.

[65] P.P. Brown, D.F. Lawler, Sphere drag and settling velocity revisited, J. Environ. Eng. 129 (3) (2003) 222–231, http://dx.doi.org/10.1061/(ASCE)0733-9372(2003)129:3(222), URL https://ascelibrary.org/doi/10.1061/%28ASCE%290733-9372%282003%29129%3A3%28222%29.

[66] A.B. Basset, A Treatise on Hydrodynamics, Deighton, Bell and Co., Cambridge, 1888.

[67] T. Young, III. An essay on the cohesion of fluids, Philos. Trans. R. Soc. Lond. 95 (1805) 65–87, http://dx.doi.org/10.1098/rstl.1805.0005, URL https://royalsocietypublishing.org/doi/10.1098/rstl.1805.0005.

[68] H. Brauer, D. Mewes, Strömungswiderstand sowie stationärer und instationärer Stoff- und Wärmeübergang an Kugeln, Chem. Ing. Tech. 44 (13) (1972) 865–868, http://dx.doi.org/10.1002/cite.330441314, URL https://onlinelibrary.wiley.com/doi/10.1002/cite.330441314.

[69] G. Haller, Lagrangian coherent structures from approximate velocity data, Phys. Fluids 14 (6) (2002) 1851–1861, http://dx.doi.org/10.1063/1.1477449, URL http://aip.scitation.org/doi/10.1063/1.1477449.
[70] G. Haller, F.J. Beron-Vera, Geodesic theory of transport barriers in two-dimensional flows, Physica D 241 (20) (2012) 1680–1702, http://dx.doi.org/10.1016/j.physd.2012.06.012, URL https://linkinghub.elsevier.com/retrieve/pii/S016727891200187X.
[71] M.E. Gurtin, An introduction to continuum mechanics, in: Mathematics in Science and Engineering, vol. 158, Academic Press, New York, 1981.
[72] V.I. Arnold, Mathematical methods of classical mechanics, second ed., [7. korr. Nachdr.], in: Graduate Texts in Mathematics, (60) Springer, New York, 2001.
[73] G. Haller, Lagrangian coherent structures, Annu. Rev. Fluid Mech. 47 (2015) 137–162.
[74] M. Serra, G. Haller, Objective Eulerian coherent structures, Chaos 26 (5) (2016) 053110, http://dx.doi.org/10.1063/1.4951720, URL https://pubs.aip.org/cha/article/26/5/053110/280323/Objective-Eulerian-coherent-structures.
[75] W.H. Beyer, Handbook of Mathematical Science, CRC Press, 2018.
[76] J.M. Rallison, The deformation of small viscous drops and bubbles in shear flows, Annu. Rev. Fluid Mech. 16 (Volume 16, 1984) (1984) 45–66, http://dx.doi.org/10.1146/annurev.fl.16.010184.000401, URL https://www.annualreviews.org/content/journals/10.1146/annurev.fl.16.010184.000401.
[77] D. Lohse, S. Grossmann, Intermittency in turbulence, Phys. A 194 (1) (1993) 519–531, http://dx.doi.org/10.1016/0378-4371(93)90382-E, URL https://www.sciencedirect.com/science/article/pii/037843719390382E.
[78] A. Mersmann, Auslegung und Maßstabsvergrößerung von Blasen- und Tropfensäulen, Chem. Ing. Tech. 49 (9) (1977) 679–691, http://dx.doi.org/10.1002/cite.330490902, URL https://onlinelibrary.wiley.com/doi/10.1002/cite.330490902.
[79] T. Krüger, H. Kusumaatmaja, A. Kuzmin, O. Shardt, G. Silva, E.M. Viggen, The Lattice Boltzmann Method: Principles and Practice, Springer Berlin Heidelberg, New York, NY, 2016.
[80] S. Succi, The lattice Boltzmann equation: For fluid dynamics and beyond, in: Numerical Mathematics and Scientific Computation, Clarendon Press, 2001, URL https://books.google.de/books?id=OC0Sj_xgnhAC.
[81] R.V. Mises, H. Pollaczek-Geiringer, Praktische Verfahren der Gleichungsauflösung, ZAMM Z. Angew. Math. Mech.- J. Appl. Math. Mech. 9 (2) (1929) 152–164, http://dx.doi.org/10.1002/zamm.19290090206, URL https://onlinelibrary.wiley.com/doi/10.1002/zamm.19290090206.
[82] M-Star Simulations, LLC., M-star CFD documentation, 2024, https://docs.mstarcfd.com/index.html. (Last Access: 10 July 2024).
[83] B. Boshenyatov, Laws of bubble coalescence and their modeling, J. Magnetohydrodyn. Plasma Res. 18 (4) (2013).
[84] P. Rehner, G. Bauer, J. Gross, FeO $_s$: An open-source framework for equations of state and classical density functional theory, Ind. Eng. Chem. Res. 62 (12) (2023) 5347–5357, http://dx.doi.org/10.1021/acs.iecr.2c04561, URL https://pubs.acs.org/doi/10.1021/acs.iecr.2c04561.
[85] E. Loth, Quasi-steady shape and drag of deformable bubbles and drops, Int. J. Multiph. Flow 34 (6) (2008) 523–546, http://dx.doi.org/10.1016/j.ijmultiphaseflow.2007.08.010, URL https://linkinghub.elsevier.com/retrieve/pii/S0301932207001711.
[86] A. Tomiyama, I. Kataoka, I. Zun, T. Sakaguchi, Drag coefficients of single bubbles under normal and micro gravity conditions, JSME Int. J. Ser. B 41 (2) (1998) 472–479, http://dx.doi.org/10.1299/jsmeb.41.472, URL http://www.jstage.jst.go.jp/article/jsmeb1993/41/2/41_2_472/_article.
[87] M. Muniz, M. Sommerfeld, On the force competition in bubble columns: A numerical study, Int. J. Multiph. Flow 128 (2020) 103256, http://dx.doi.org/10.1016/j.ijmultiphaseflow.2020.103256, URL https://linkinghub.elsevier.com/retrieve/pii/S030193221930535X.
[88] M. Sommerfeld, Bewegung fester Partikel in Gasen und Flüssigkeiten, in: P. Stephan, D. Mewes, S. Kabelac, M. Kind, K. Schaber, T. Wetzel (Eds.), VDI-Wärmeatlas : Fachlicher Träger VDI-Gesellschaft Verfahrenstechnik und Chemieingenieurwesen, Springer Berlin Heidelberg, Berlin, Heidelberg, 2018, pp. 1–17, http://dx.doi.org/10.1007/978-3-662-52991-1_88-2.
[89] J. Urizarna-Carasa, D. Ruprecht, A. von Kameke, K. Padberg-Gehle, Relevance of the basset history term for Lagrangian particle dynamics, 2024, URL http://arxiv.org/abs/2407.01041, arXiv:2407.01041 [physics].
[90] J. Urizarna-Carasa, L. Schlegel, D. Ruprecht, Efficient numerical methods for the maxey-riley equations with basset history term, 2024, URL http://arxiv.org/abs/2403.13515, arXiv:2403.13515 [cs, math].